

# Destruction and regrowth of lithospheric mantle beneath large igneous provinces

Simon N. Stephenson,<sup>\*,1</sup>, Patrick W. Ball,<sup>2</sup> & Fred D. Richards,<sup>3</sup>

1. Department of Earth Sciences, University of Oxford, Oxford, UK.
2. Department of Geosciences, Colorado State University, Fort Collins, Colorado, USA.
3. Department of Earth Science and Engineering, Imperial College London, London, UK

\*simon.stephenson@earth.ox.ac.uk

## **Abstract**

Large igneous provinces (LIPs) are formed by enormous (i.e. frequently  $> 10^6 \text{ km}^3$ ), but short-lived magmatic events that have profound effects upon global geodynamic, tectonic, and environmental processes. Lithospheric structure is known to modulate mantle melting, yet its evolution during and after such dramatic periods of magmatism is poorly constrained. Using geochemical and seismological observations, we find that magmatism is associated with thin (i.e.  $\lesssim 80 \text{ km}$ ) lithosphere and we reveal a striking positive correlation between the thickness of modern-day lithosphere beneath LIPs and time since eruption. Oceanic lithosphere re-thickens to 125 km, while continental regions reach  $> 190 \text{ km}$ . Our results point to systematic destruction and subsequent regrowth of lithospheric mantle during and after LIP emplacement and re-cratonisation of the continents following eruption. These insights have implications for the stability, age and composition of ancient, thick, and chemically distinct lithospheric roots, the distribution of economic resources, and emissions of chemical species that force catastrophic environmental change.

## 12    1 Introduction

13    The thermomechanical structure of the lithospheric plate and its interaction with the underlying asthenosphere influence  
 14    the evolution of Earth's topography, plate motions and deformation, the pattern of mantle convection, and the location and  
 15    style of volcanism (1–5). Consequently, lithospheric evolution drives erosional and depositional processes, controls the  
 16    distribution of economic resources, and influences climatic and environmental conditions through space and time (6–9).  
 17    Geological and geophysical observations provide constraints on present-day lithospheric structure, but only snapshots of  
 18    its variations through time [e.g. (8, 10–15)].

19    It is often assumed that the lithospheric structure of ancient continental interiors (i.e. cratons) is stable and unchanging  
 20    over very long time periods, yet there is a paucity of data with which to test this hypothesis [see (16) for a comprehensive  
 21    review]. In general, this belief stems from the exposure of exclusively ancient, undeformed shields at low-elevations with  
 22    low relief that overlie thick (i.e.,  $\gtrsim 200$  km), depleted lithosphere that is intrinsically buoyant, viscous, and therefore  
 23    difficult to convectively remove (5, 17–19). However, several of these cratons are capped by Phanerozoic large igneous  
 24    provinces (LIPs) — giant outpourings of lava ( $> 10^6$  km $^3$ ) that were extruded within geologically short time frames  
 25    ( $< 5$  Myr) — which are commonly linked to the arrival of plume heads beneath the plate (20). For example, the Siberian  
 26    Traps, Central Atlantic Magmatic Province, and Karoo flood basalts overlie the Siberian, West African, and Kalahari  
 27    cratons, respectively. This association calls into question the assumption that cratonic lithosphere is thick and stable since  
 28    a thin tectonic lid is required to generate large volumes of melt, and present-day magmatism is strongly associated with  
 29    lithosphere  $< 100$  km thick (1, 21–24).

30    In this contribution, we attempt to reconcile these seemingly contradictory observations by tracking lithospheric  
 31    evolution during and after magmatism. We begin by comparing the locations and ages of modern and ancient oceanic  
 32    islands, seamounts and plateaux to estimates of plate age and lithospheric thickness. Subsequently, this analysis is  
 33    extended into continental regions, where we develop conceptual and numerical models to explain the lithospheric response  
 34    to intraplate magmatic events. Finally, we describe the implications of our results for the thermochemical structure of  
 35    cratonic lithosphere and their use in addressing several key geodynamic, economic and environmental questions.

## 36    2 Results

### 37    2.1 Oceanic Intraplate Magmatism

#### 38    2.1.1 Recent Intraplate Magmatism

39    Our starting point is to explore lithospheric thickness beneath modern-day intraplate magmatic provinces. In the oceanic  
 40    realm, the lithospheric mantle cools and thickens away from mid ocean ridges in a predictable way (10, 25–28). This  
 41    phenomenon is one of the most widely accepted and well studied in global geophysics. Usefully, it allows expected  
 42    time-dependent deepening of the lithosphere-asthenosphere boundary (LAB) to be used as a reference template against  
 43    which deviations in lithospheric thickness can be defined and explored.

44    We wish to determine whether intraplate magmatism is associated with deviations from the plate-cooling relationship.  
 45    To carry out this test, we exploit a global database of intraplate magmatic analyses (22). This compilation includes major  
 46    and trace geochemical compositions of mafic rocks at all locations where intraplate magmatism has occurred within the  
 47    last 10 Ma and has not since moved further than 400 km from the site of eruption (Figure 1a). We estimate modern-day  
 48    depth to the LAB,  $z_{LAB}^1$ , beneath each recent intraplate magmatic province in three ways. First, LAB depth beneath  
 49    each location is extracted from the lithospheric thickness model of Hoggard *et al.* (8), which is located by contouring  
 50    the 1175 °C isothermal surface after converting the SL2013sv shear-wave tomographic model into temperature (Figure  
 51    1b). This temperature conversion scheme exploits a calibrated elastic-anelastic parameterisation (28). Secondly, we use

the lithospheric thickness estimates calculated by inverse modelling of rare earth element concentrations within mafic intraplate magmas carried out by Ball *et al.* (22)(see Methods). This method is predicated upon the partitioning of rare earth elements between mantle melt and residue during partial melting, where the upper limit of melting is taken to represent the LAB. Finally, we estimate the depth to the LAB by calculating melt equilibration pressure,  $P_{eq}$ , and temperature,  $T_{eq}$ , of intraplate melts using the thermobarometric scheme developed by Plank *et al.* (29). This scheme exploits the sensitivity of major oxide phase concentrations within mafic melts to these two properties within the mantle [e.g. (29, 30), See Methods]. The global database of Ball *et al.* (22) is filtered for samples where  $9 < \text{MgO} < 14.5 \text{ wt\%}$  in order to mitigate removal or addition of material by fractionation or contamination. Then  $T_{eq}$  and  $P_{eq}$  are calculated for the remaining samples. We locate samples that equilibrated beneath the LAB by selecting samples where  $T_{eq} > 1175^\circ\text{C}$ . This screening procedure ensures consistency with tomographically determined LAB depths. Next, samples are geographically divided into  $1 \times 1^\circ$  bins. We exclude bins with < 10 samples since it is unlikely that a very small sample size can be used to accurately locate the base of the lithosphere. Finally, the minimum value of  $P_{eq}$  is calculated within each bin, which enables an approximation of maximum depth to the LAB (i.e.  $z_{LAB} \approx 31.4 P_{eq}^{min}$ ).

Figure 1c shows the three independent estimates of LAB depth,  $z_{LAB}^1$ , beneath recent oceanic intraplate magmatic provinces. In this case, we present our results as a function of the age of oceanic crust atop which the magmatic provinces rest (8, 31). All else being equal, the depth to the LAB beneath these provinces should be governed entirely by plate cooling as a function of oceanic crustal age. These constraints are therefore compared to two estimates of unperturbed LAB depth. First, we calculate predicted LAB depth using a plate-cooling model constructed by Richards *et al.* [i.e. black line on Figure 1c (28)]. Secondly, we compare to the global median LAB depth as a function of oceanic crustal age determined by Hoggard *et al.* [i.e. black circles on Figure 1c (8)]. These two estimates of expected  $z_{LAB}^1$  values are in close agreement, although it is important to note that they are not entirely independent of one another [see (8, 27, 28)].

For magmatic provinces located above young oceanic crust (i.e.  $t_{crust} < 30 \text{ Ma}$ ), predictions and observations are in close agreement, indicating that  $z_{LAB}^1$  increases from  $\sim 20\text{--}50 \text{ km}$  to  $60\text{--}80 \text{ km}$  during this time period. For crustal ages  $t_{crust} > 30 \text{ Ma}$ , however, expected and observed LAB depths beneath intraplate magmatic provinces dramatically diverge. For an oceanic crustal age,  $t_{crust} \gtrsim 30 \text{ Ma}$ , the plate is systematically thinner by  $30\text{--}60 \text{ km}$  than would be expected given the crustal age (compare black line and circles with coloured symbols on Figure 1c). These observations suggest that magmatism occurs exclusively where  $z_{LAB} < 100 \text{ km}$ , and in most cases only where,  $z_{LAB} \lesssim 80 \text{ km}$ .

To make sense of this relationship, consider first the Icelandic hotspot. This magmatic province straddles the Mid-Atlantic Ridge, where lithospheric mantle is thin or absent due to active sea-floor spreading. Consequently, all lithospheric thickness proxies suggest that melts are able to ascend to a shallow level, unimpeded by the presence of lithospheric mantle, before encountering the Moho at depths of  $\sim 15\text{--}45 \text{ km}$  (32, 33). Next, consider the Hawaiian hotspot, which has  $t_{crust} \sim 90 \text{ Ma}$ . The LAB ought to be found at  $z_{LAB}^1 \approx 100 \text{ km}$  according to both predicted plate cooling and the global average for oceanic lithosphere of that age. However, major oxide concentrations suggest that Hawaiian melts equilibrate within the asthenosphere to depths as shallow as  $30\text{--}60 \text{ km}$  (see yellow stars on Figure 1c). Furthermore, rare earth element inverse modelling suggests that the top of the asthenospheric melt column is located at  $40\text{--}60 \text{ km}$  depth (see red squares on Figure 1c). Finally, local and global seismic imaging indicates that beneath Hawaii  $z_{LAB}^1 \sim 40\text{--}90 \text{ km}$  [e.g. (8, 34, 35), see green triangles on Figure 1c]. This thinner lithosphere is in keeping with flexural and gravimetric observations, as well as with xenolith-based thermobarometric results which indicate that temperatures of  $1000\text{--}1100^\circ\text{C}$  occur at depths of  $45\text{--}55 \text{ km}$  beneath Hawaii (36, 37). In contrast to the Icelandic example, this discrepancy suggests that, locally,  $z_{LAB}^1$  is significantly shallower than expected beneath Hawaii. Taken together, these considerations strongly suggest that when the plate thickens beyond  $70\text{--}80 \text{ km}$  (i.e. when  $t_{crust} \gtrsim 30 \text{ Ma}$ ), magmatism is associated with marked lithospheric thinning to depths of  $60\text{--}80 \text{ km}$ . In other words magmatism appears to reset  $z_{LAB}$  to depths found beneath oceanic crust with an age of  $\sim 20\text{--}40 \text{ Ma}$ .

### 95 2.1.2 Ancient Intraplate Magmatism

96 Following cessation of magmatism, lithosphere that is < 80 km thick should re-thicken as a result of conductive cooling.  
 97 Modern-day LAB depth,  $z_{LAB}^1$ , should therefore be thicker beneath older intraplate magmatic provinces than those  
 98 erupting at present. We test this hypothesis by substantially updating a global map of oceanic plateaux, islands and  
 99 seamounts [ (38, 39); Figure 1b; Dataset S1]. This database contains polygons outlining these oceanic landforms and an  
 100 associated eruption age,  $t_e$ , of the magmatic rocks that form them. Polygons are added, excluded and their age constraints  
 101 updated according to the recent literature (see Supplementary Information). We sample modern-day depth to the LAB  
 102 at  $0.1 \times 0.1^\circ$  intervals beneath each polygon in our updated database. Once again, we exploit estimates of lithospheric  
 103 thickness calculated by Hoggard *et al.* (8). Next, for each polygon, we carry out two tests (see Methods). First, we test  
 104 whether another volcanic province lies either inside, or within 500 km of the polygon outline of interest. Secondly, we test  
 105 whether any polygon passing the first test is more than 30 Myr younger in age than the polygon of interest. Should  
 106 both tests be passed, we excise the polygon of interest. This filtering procedure ensures that only the effects of passive  
 107 lithospheric thickening following the final volcanic episode are captured, thus avoiding contamination by subsequent  
 108 magmatism-associated lithospheric thinning. We calculate the moving median and interquartile range of  $z_{LAB}^1$  values  
 109 beneath the remaining intraplate magmatic provinces as a function of  $t_e$ . In calculating each median value, we weight  
 110 the  $z_{LAB}^1$  value of each point as a function of latitude in order to avoid biasing moving average estimates towards polar  
 111 provinces (see Methods).

112 Figure 1d, black circles with error bars, shows observed values of  $z_{LAB}^1$  as a function of  $t_e$ . The median LAB depth  
 113 beneath the youngest provinces (i.e. where eruption age,  $t_e < 10$  Ma) are consistent with the median thickness calculated  
 114 for the database of Ball *et al.* (22). Importantly, we find that there is a positive relationship between province age and LAB  
 115 depth beneath the province up to an age of  $\sim 80$ –100 Ma, at which point the deepening of  $z_{LAB}^1$  flattens off (see black  
 116 circles with error bars on Figure 1d). The shape of this relationship resembles a plate cooling model that flattens at a depth  
 117 consistent with several well-known, published schemes [i.e. 100–130 km; Figure 1c and d; (10, 27, 40, 41)].

118 Since older oceanic plate is associated with thicker lithosphere, it is possible that any positive relationship between  
 119  $z_{LAB}^1$  and  $t_e$  is generated by chance. This general trend could be produced by distributing intraplate magmatism randomly  
 120 upon a lithospheric plate whose thickness is governed solely by plate cooling as a function of oceanic crustal age. This  
 121 relationship would arise because provinces with an eruption age of, say,  $t_e = 180$  Ma can only possibly be found today  
 122 on old lithosphere, which in the absence of any thermal perturbation would be around 125 km thick [e.g. (27)]. However,  
 123 recent intraplate magmatism (i.e.  $t_e = 0$  Ma) could theoretically be distributed over lithosphere of thickness ranging from  
 124 zero at a mid-ocean ridge to 125 km on the abyssal plain. The median LAB depth of this distribution would therefore  
 125 be thinner than for those locations overlying only older oceanic crust. As a result, even if  $z_{LAB}^1$  is controlled only by  
 126 oceanic crustal age, younger intraplate magmatism is be expected to overlie, on average, thinner lithosphere than sites of  
 127 older magmatism. A sample of young seamounts, islands and plateaux would also have a broader distribution of  $z_{LAB}^1$   
 128 values than older provinces. However, if magmatic emplacement is associated with systematic thinning of the plate (i.e.  
 129 shallowing of the LAB), then observed values of  $z_{LAB}^1$  beneath oceanic plateaux, islands and seamounts ought to be  
 130 systematically thinner for any  $t_e < 80$ –100 Ma than the  $z_{LAB}^1$  values expected from plate cooling alone.

131 To investigate whether temporal trends in  $z_{LAB}^1$  provide evidence for magmatism-related lithospheric thinning, we  
 132 calculate the expected, thermally unperturbed  $z_{LAB}^1$  distribution beneath a random sample of oceanic islands, seamounts  
 133 and plateaux as a function of  $t_e$  given plate cooling alone (see Methods). As expected, we find that, indeed, there is a slight  
 134 positive relationship between plate age and unperturbed lithospheric thickness beneath ancient oceanic magmatic provinces  
 135 (see blue line and envelope on Figure 1d). This predicted distribution is then compared to the observed distribution (i.e.  
 136 black circles with error bars on 1d). Importantly, up to an eruption age,  $t_e \approx 90$  Ma, ancient magmatic provinces  
 137 systematically overlie lithosphere that is  $\sim 20$ –40 km thinner than would be expected if the plate were not perturbed since

138 sea-floor spreading (compare black circles and blue line on Figure 1d). This result is not materially affected by using  
 139 alternative lithospheric thickness models (see Supplementary Material). This finding further supports our earlier insight  
 140 that intraplate magmatism resets the plate cooling process by thinning the lithospheric mantle. It is also consistent with  
 141 seminal work by Detrick & Crough (42), who showed that ocean island subsidence cannot be explained only by seafloor  
 142 age, and instead requires lithospheric thinning and time-dependent re-thickening. Intriguingly, our results suggest that the  
 143 thickness of the plate beneath ancient seamounts and plateaux may be predicted using the eruption age of the province and  
 144 should not be predicted by oceanic crustal age.

## 145 2.2 Continental Large Igneous Provinces

146 The time-dependent re-thickening of oceanic lithosphere following eruption of seamounts raises an important question:  
 147 does continental lithosphere behave in a similar way? Answering this question is complicated by the fact that lithospheric  
 148 thicknesses in the continental realm do not generally appear to follow a predictable age-dependent relationship. Neverthe-  
 149 less, Ball *et al.* (22) demonstrated that geochemical and seismological constraints require thin lithosphere beneath almost  
 150 all recent continental intraplate magmatic provinces, while White & M<sup>c</sup>Kenzie (43) used a similar approach to show that  
 151 ancient provinces are also associated with thin lithosphere at the time of their formation. We therefore return to our updated  
 152 database of intraplate magmatic provinces to explore whether the relationship between  $z_{LAB}$  and intraplate magmatism  
 153 also applies to the continents. On the continents, this database is mostly comprised of large igneous provinces (LIPs), a  
 154 dominance that is particularly acute prior to Cenozoic times. As in the oceanic realm, we have updated the database to  
 155 amend province ages and polygon outlines, while also including provinces up to 750 Ma [e.g. (20); see Supplementary  
 156 Information]. Similarly, we also exclude any location where subsequent magmatism occurred within 500 km of the  
 157 eruption site after 30 Myr of the initial eruption so that only the final phase of intraplate magmatism is included in our  
 158 database. We again sample  $z_{LAB}^1$  within each polygon at  $0.1 \times 0.1^\circ$  intervals.

159 Figure 2 shows depth to the LAB beneath continental LIPs as a function of time. For the first time, we reveal a striking  
 160 relationship between lithospheric thickness and continental LIP age. For recent provinces, the lithosphere is  $\sim 50$  km thick,  
 161 which is consistent with that observed in the oceans and a range of geochemical proxies for lithospheric thickness (22).  
 162 LAB depth increases to approximately 190 km at 250 Ma before flattening off. For example, the Ethiopian Flood Basalts  
 163 were erupted at  $\sim 30$  Ma, with magmatism continuing to recent times, and are underlain by lithosphere that is  $< 50$  km  
 164 thick (22, 44). The 138–128 Ma Paraná-Etendeka Traps, on the other hand, are underlain by lithosphere that is 100–150 km  
 165 thick. However, 190 km-thick lithosphere underlies the Siberian traps, which was erupted at 250 Ma. This thickness is  
 166 similar to the LAB depth beneath the 510 Ma Kalkarindji LIP in central and northwestern Australia, and the 750 Ma  
 167 Franklin LIP in the Canadian Arctic. The Deccan Traps (66 Ma) mark the only significant outlier to this relationship,  
 168 having markedly thicker lithosphere than LIPs of a similar age. Significantly, the depth at which  $z_{LAB}^1$  stops increasing and  
 169 flattens off (i.e.  $\sim 190$  km) is about 60–90 km deeper than that observed for the oceans (compare Figures 1d, black circles  
 170 and 2b). It is important to note that our analysis encompasses LIPs erupted onto all types of continental environments,  
 171 ranging from shields (e.g. eastern Siberian Traps) to Phanerozoic sediments (e.g. Central Atlantic Magmatic Province,  
 172 i.e., CAMP, and Karoo).

## 173 2.3 Thermal Modelling

174 It is clear that intraplate magmatism occurs above thinner-than-expected lithosphere and that older magmatic provinces  
 175 reside above progressively thicker lithosphere. Rifting, which leads to rapid thinning of the lithosphere (i.e. shallowing  
 176 of the LAB), is usually followed by protracted time-dependent re-thickening as a result of conductive cooling. Similarly,  
 177 the systematic increase in LAB depth beneath magmatic provinces from young to old suggests that the plate thickens as  
 178 a function of time following the cessation of magmatism. This deepening eventually stalls and flattens out at a constant

thickness of around  $\sim 190$  km beneath continental provinces and  $\sim 125$  km in the oceans. Two principal models have been developed to explain time-dependent thickening of the lithospheric plate. First, a half-space model, in which the lithosphere cools and thickens indefinitely as a function of age, and secondly a plate model, in which the lithosphere cools and thickens, initially closely matching the half-space model, before approaching a finite thickness controlled by the convective resupply of basal heat [e.g. (10, 40, 45)]. The impact of this heating is generally approximated by imposing a constant basal potential temperature,  $T_p$ , at a particular depth,  $z_p$ , that defines the maximum depth to which conductive cooling can penetrate (27, 46). Note that  $z_p$  is not the same as  $z_{LAB}$ . Here we investigate whether conductive cooling, represented in this case by a plate model, can explain the time-dependent thickening of the lithosphere,  $z_{LAB}(t)$ , following intraplate magmatism.

### 2.3.1 Oceanic Intraplate Magmatic Provinces

Again we begin with the oceanic lithosphere. We model 1D thermal evolution,  $T(z, t)$ , beneath LIPs and hence depth to the LAB as a function of time,  $z_{LAB}(t)$ , by making three simple modifications to the plate model of Richards *et al.* (27, 46). First, rather than assuming an initial temperature profile consistent with mid-ocean ridge conditions (i.e., LAB depth  $\sim 10$  km below sea-level), a steady-state initial temperature profile with an LAB depth equal to 50 km is imposed, so that  $z_{LAB}^0 = 50$  km when magmatism occurs. In practice, this constraint means initially placing the  $1175\text{ }^\circ\text{C}$  isotherm at a depth of 50 km. This assumption is consistent with both the results of our geochemical modelling and tomographically constrained LAB depth beneath intraplate magmatic provinces. Secondly, we assume that the less conductive oceanic crustal layer is 20 km rather than 7 km thick, a choice that reflects elevated thickness beneath magmatic provinces relative to standard oceanic crust. Finally, observational studies have strongly suggested that initial excess subsidence of ocean islands is generated by movement away from swell bathymetry that is at least partly generated by excess mantle temperatures (47). Hence, to account for the excess heat provided by a putative mantle plume, initial steady-state temperature profiles corresponding to elevated initial mantle potential temperature,  $(T_p)_0$ , are imposed. As the thermal structure evolves,  $(T_p)_0$  decays linearly over time (30 Myr) to the ambient mantle value adopted by Richards *et al.*,  $T_p = 1333\text{ }^\circ\text{C}$  [see Methods, (46)]. This evolving temperature excess is initially imposed at the base of the thermal boundary layer (i.e., the shallowest depth at which  $\frac{dT}{dz}$  drops below  $0.5\text{ }^\circ\text{C km}^{-1}$ ), before deepening at a rate of  $10\text{ mm yr}^{-1}$ . This progressive temperature decay and vertical advection of the thermal boundary simulate the movement of the plate away from a plume-like mantle heat source (47). To find the optimum plate model that best describes our  $z_{LAB}(t)$  observations, we carry out a grid search in which pairs of  $z_p$  and  $(T_p)_0$  are systematically explored and optimized.

Our results show that cooling and re-thickening of the lithosphere from an initial thickness of  $\sim 50$  km following the cessation of magmatism can explain the distribution of oceanic LAB depth as a function of time. Importantly, the optimal plate thickness is closely comparable to that obtained by fitting global oceanic bathymetry and heat flow data as a function of plate age (27, 46). The significant difference is that while the best-fitting value of  $z_p$  is only  $\sim 17 \pm 10$  km in excess of that required to explain global oceanic subsidence and heat flow, an initial excess temperature anomaly of between 0 and  $+200\text{ }^\circ\text{C}$  relative to the global background is required to fit  $z_{LAB}(t)$  beneath intraplate magmatic provinces [Figure 3a; (46)]. This temperature anomaly then wanes rapidly. This result is consistent with both excess asthenospheric potential temperatures associated with at least some proportion of intraplate magmatism and constraints from the drowning of ocean islands (22, 43, 47).

### 2.3.2 Continental Large Igneous provinces

Next we extend this model to the continental realm. First, we maintain the condition that the initial LAB depth is 50 km (i.e.  $z_{LAB}^0 = 50$  km). This assumption is supported by modelling of rare earth element compositions of mafic and ultramafic melts in LIP magmas (43). Secondly, we assume that continental crustal thickness,  $z_{cc} = 35$  km, and

account for differences in thermal properties associated with its more felsic composition including enhanced radiogenic heat production,  $H^*$ , and higher thermal conductivity [see Methods; (48)]. As before, the initial temperature profile is determined by finding the steady state geotherm, given the value of  $(T_p)_0$ , that results in the 1175 °C isotherm at a depth of 50 km. We carry out a grid search to determine the best-fitting values of  $(T_p)_0$  and  $z_p$  that are consistent with observed values of  $z_{LAB}$  as a function of LIP age. The Deccan Traps are excluded from our analysis since its two contributing temporal bins are clear outliers.

Results show that, as for the oceans, the thickness of the lithospheric mantle beneath continental LIPs can be fitted with a simple adapted plate-cooling model, although with some significant differences. Importantly, the best-fitting potential temperature is  $(T_p)_0 = 1483 \pm 120$  °C, which, while less well defined, overlaps with the range of values of  $(T_p)_0$  in the oceanic realm (Figure 3). Indeed, these results suggest that significantly elevated mantle potential temperatures (i.e.  $(T_p)_0 > 1360$  °C) are a systematic requirement of LIP formation, providing independent evidence for their formation above a mantle plume (43, 49, 50). However, the optimal plate thickness,  $z_p = 243$  km, is significantly greater than in the oceans, which implies a steady-state LAB depth of  $z_{LAB}^\infty \approx 192$  km. This depth is closer to lithospheric thicknesses implied by subsidence in intra-cratonic rift basins (i.e. ~ 200 km) than either in standard rift basins on less ancient continental lithosphere or in the oceanic realm [i.e. ~ 100–150 km; (51, 52)]. Note that, although we have chosen to exclude the Deccan Traps outliers from our analysis, the best-fitting value of  $z_p$  is minimally affected by their inclusion (i.e., an increase of 2 km), while optimal  $(T_p)_0$  remains ~ 80 °C above ambient values (i.e., 1415 °C versus 1333 °C; see Supplementary Material).

In summary, our modelling results suggest that the lithospheric mantle is rapidly thinned immediately prior to and/or during magmatism. It then cools and progressively re-thickens following magmatism. For continental LIPs, this thinning is associated with a significant temperature anomaly and steady-state plate thicknesses are similar to those in intra-cratonic basins.

### 3 Discussion

Our global analysis of lithospheric thickness beneath intraplate magmatic provinces has shown that magmatism occurs exclusively on thin lithosphere. Following eruption, the lithospheric mantle progressively cools and re-thickens to a depth of 125 km in the oceans and 190 km on the continents. These inferences are supported by a range of observations. First, major and trace elemental compositions of recent intraplate magmas suggest that magmatism occurs only where the lithosphere is less than 80 km thick. Secondly, the thickness of the lithospheric plate calculated from a calibrated  $V_S$ -to- $T$  conversion that is based upon the SL2013sv shear-wave velocity model is in broad agreement with these geochemical estimates. Thirdly, the thickness of the lithosphere beneath ancient intraplate magmatic provinces is systematically thinner than would be expected if they were randomly distributed atop oceanic lithosphere that was following the well-documented plate-cooling relationship. Finally, lithospheric thickness defined by seismic tomographic imaging beneath both oceanic and continental intraplate magmatic provinces systematically increases as a function of eruptive age following a plate cooling relationship subject to initially elevated asthenospheric temperatures. A key observation is that several continental LIPs overlie cratons, which are regions of supposedly ancient, thick, and stable lithospheric mantle (e.g. Karoo, CAMP, Emeishan, Siberia, Kola-Dnieper, Kalkarindji, Franklin). Our results suggest that even cratonic continental interiors are significantly less stable than often assumed, with cratonic roots apparently neither able to resist being destroyed during LIP emplacement, nor remaining permanently thinned after the cessation of magmatism. Here we discuss the implications of the relationship between LIP emplacement, rapid lithospheric thinning and protracted thermal relaxation for the compositional make-up of continental lithosphere through time, the formation of economic resources, and the initiation of mass extinction events.

### 261 3.1 Re-cratonisation

262 Previous insights indicate that thick, cratonic lithosphere is likely to have been generated by high degrees of melt extraction  
 263 at shallow depths followed by lithospheric thickening during ancient (i.e. pre-Phanerozoic) orogenic events [refs (16, 53)  
 264 and references therein]. Our results, however, suggest that in some locations, this pre-existing lithospheric mantle is  
 265 destroyed prior to, or during, LIP eruption. It is then re-emplaced over the subsequent  $\sim 300$  Ma by thermal relaxation  
 266 (Figure 2b and 3d). Compositional differences between unperturbed and re-thickened cratonic lithosphere are challenging  
 267 to distinguish geophysically. However, our results allow useful constraints to be placed upon the compositional evolution  
 268 of cratonic roots during and after magmatism.

269 LIPs often appear on ancient cratons (e.g. Siberia, Karoo, Central Magmatic Igneous Province, Franklin), which are  
 270 likely to have depleted, low-density lithospheric roots (17). Thinning of undepleted lithospheric mantle is a significant  
 271 means of generating topographic uplift and denudation on  $10^3$  km lengthscales (54). Conversely, thickening of an  
 272 undepleted lithospheric root drives time-dependent subsidence (55). Lithospheric depletion (i.e. density reduction,  
 273  $\Delta\rho$ ) modulates the amplitude of this uplift and subsidence. Consider a cratonic setting where the onset of magmatism  
 274 is associated with a combination of a transient asthenospheric thermal anomaly and removal of an ancient, thermally  
 275 equilibrated, and depleted (i.e. low-density) cratonic root (Figure 4a–b). In this case, the initial density of the root,  $\rho_m^*$   
 276 is perhaps  $50 \text{ kg m}^{-3}$  lower than in Phanerozoic lithospheric mantle. Removal of this depleted root leads to significant  
 277 amounts of surface uplift (i.e.  $U_o = 1.8 \text{ km}$  if  $(T_p)_0 = 1483^\circ\text{C}$ , see Methods). Note that if  $\rho_m^*$  is significantly more  
 278 depleted, then the magnitude of this uplift decreases substantially (e.g. around  $\sim 500 \text{ m}$  for depletion of  $80 \text{ kg m}^{-3}$ ).  
 279 Subsequent thermal re-equilibration drives re-growth of the lithospheric mantle (Figure 4c–g). If this lithospheric mantle  
 280 is completely undepleted, then the result is net air-loaded subsidence of  $1.6 \text{ km}$  after 350 Ma and  $2.1 \text{ km}$  after 750 Ma.  
 281 No net uplift or subsidence occurs when re-thickening mantle lithosphere is depleted by  $50 \text{ kg m}^{-3}$  (i.e. same density  
 282 as precursor lithospheric mantle,  $\rho_m^*$ ). Finally, if depletion is increased to  $80 \text{ kg m}^{-3}$  then a total of  $1.3 \text{ km}$  net uplift is  
 283 generated after 750 Ma (Figure 4f and g; Methods).

284 Extensive evidence exists for uplift associated with intraplate magmatism although in cratonic regions it can be  
 285 controversial. [e.g. (22, 50, 56–59)]. This controversy perhaps indicates the relatively modest magnitude of initial uplift  
 286 expected as a result of rapid thinning of depleted cratonic lithosphere. This more modest magnitude is in contrast to the  
 287 kilometre-scale uplift expected above more fertile lithosphere [e.g. (15, 54, 60, 61)]. A second important observation is that  
 288 many LIPs are exposed at the surface today and not buried under deep sedimentary basins. It is therefore likely that they  
 289 have experienced either uplift or at least neutral net vertical motion since the end of magmatism. Taken together with the  
 290 results of our simple modelling, these observations suggest that depleted cratonic lithosphere is removed before or during  
 291 magmatism, then it is replaced by similarly, or more depleted lithospheric mantle during subsequent thermal relaxation.  
 292 LIP emplacement therefore provides a mechanism for cratonic destruction followed by re-cratonisation.

293 It is important to note that all that remains of many LIPs is the plumbing system, the flood basalts having been totally  
 294 denuded (62, 63). The initial asthenospheric thermal pulse and lithospheric removal generates excess topography that is  
 295 progressively eroded (64). Similarly many, but not all, LIPs are associated with lithospheric extension. In both cases,  
 296 thinner crust will result in net subsidence after thermal re-equilibration of the lithosphere. Consequently, in order for LIP  
 297 plumbing systems to be exposed at the surface and not buried under kilometres of sediment, then post-LIP topography must  
 298 be permanently sub-crustally supported. A likely candidate for this topographic support is lithospheric depletion, which  
 299 could be modulated by magmatic underplating. An important corollary is that initial uplift, erosion, and replacement of  
 300 depleted lithospheric mantle with a less depleted subsequent lithospheric keel could be a way to generate intra-cratonic  
 301 basins.

302 In summary, it is likely that LIP emplacement drives local to regional cratonic destruction on short timescales and  
 303 re-cratonisation on long timescales. Simple geodynamic arguments support this conclusion. Equilibrium thickness of the

undepleted continental lithospheric mantle is around 100–150 km (51, 55). We find that the equilibrium thickness of the thermal boundary layer in continental regions affected by large igneous province emplacement is closer to 180–220 km. McKenzie & Richter (65) showed that the thickness of the upper thermal boundary layer,  $\delta$ , is proportional to  $\nu^{\frac{1}{3}}$ , where  $\nu$  is kinematic viscosity (i.e.  $\eta/\rho$ , where  $\eta$  is dynamic viscosity and  $\rho$  is density). At a given temperature, melt depletion leads to an increase in viscosity of the mantle residue [e.g. (66, 67)]. Hence a doubling of  $\nu$  leads to an increase in  $\delta$  of around one quarter. Geochemical depletion of the uppermost mantle therefore leads to a thickening of the upper thermal boundary layer relative to ambient mantle.

Importantly, this excess deepening is not observed in the oceanic realm, where  $z_{LAB}^\infty = 125$  km, despite similar excess mantle temperatures and comparably large melt volumes (Figure 3). In the oceans, magmatic provinces were erupted above initially thinner lithosphere than in cratonic continental regions. Numerical modelling carried out by Liu *et al.* (24) indicates that lithospheric thin spots surrounded by thick cratonic lithosphere can trap accumulations of low-density, depleted mantle material that are generated by melt extraction during LIP formation or are parcels of previously removed lithospheric mantle. Their results show that in these circumstances the lithosphere can recover up to 90% of its original thickness as it cools over the subsequent 300 Ma, almost entirely healing the initially destroyed precursory cratonic lithospheric mantle. By contrast, their analysis implies that when LIPs are emplaced in oceanic regions distant from thick cratonic lithosphere, melt-depleted material is entrained into the deep mantle, limiting the eventual re-thickening of the oceanic lithosphere. Our observations strongly support this idea and suggest that plume-driven re-cratonisation is routine in the continental realm. A caveat may therefore be that LIP emplacement is associated with re-cratonisation but is not necessarily a primary means for creating thick new cratonic roots.

### 3.2 Economic Resources

Our results provide a predictive framework for modelling the thermal evolution of undeformed continental interiors in response to magmatic events. The thinning and rethickening pattern can act as a useful tool to highlight and evaluate prospects for heat flow-dependent economic resources such as minerals and hydrocarbons. For example, diamonds primarily form within cold, thick continental lithospheric roots (i.e.,  $1130 \pm 120$  °C at  $5.3 \pm 0.8$  GPa) and are brought to the surface within kimberlite pipes (68). Our results suggest that thinning of the plate during/prior to emplacement of an LIP will suppress diamond formation and entrainment for  $\sim 300$  Myr as the plate rethickens beyond  $\gtrsim 170$  km (Figure 2b). Several LIPs are spatially proximal to older, diamondiferous and/or younger, barren kimberlite fields. These include the Siberian Traps, which erupted 75–45 Myr after the diamondiferous Alakit, Upper Muna and Daldyn fields and 0–30 Myr before the barren, traps-related Kharamay field (69). The Keweenawan LIP on the southern Superior craton, North America, at 1150–1100 Ma preceded/coincided with the barren 1100 Ma Kyle Lake kimberlite field but, crucially, the much more recent Attawapiskat kimberlites, which occurred in the same location at 180–150 Ma, were diamondiferous (70). Similar logic applies to the Artemisia kimberlites, which became diamondiferous 600 Ma after emplacement of the MacKenzie Flood Basalts above the Slave Craton, Canada (24). Previous authors have tied these relationships to the heating of lithospheric roots out of the diamond-bearing window by mantle plumes during LIP events (70–72). We contend that rapid and wholesale lithospheric removal is a key mechanism. Moreover, our observations reveal a predictive timescale over which cratonic keels will return to a state favourable to diamond formation, which is similar to results of previous modelling studies [ $\sim 300$  Myr, (24)].

### 3.3 Climate Change and Mass Extinctions

Finally, our results have implications beyond the solid Earth since LIP eruptions release large quantities of chemical species that can lead to global environmental change. When carbon, sulfur, and halogens are expelled into the atmosphere, they warm the planet, cool the planet, and deplete the ozone layer, respectively (73). The rapid and large-scale eruption of these

345 climate-forcing gases during LIP emplacement is thought to be responsible for many of Earth's mass extinctions (7, 74, 75).  
346 The Siberian Traps ( $\sim 1\text{--}2 \times 10^6 \text{ km}^3$ ) coincides with the largest known extinction event, which defines the Permian-  
347 Triassic boundary and represents the loss of > 80% of marine species (76). However, conventional mantle plume-derived  
348 melts are insufficiently concentrated in C, S, and halogens to generate the catastrophic environmental change required  
349 to drive such a mass extinction (4, 73). Metasomatized continental lithospheric mantle, on the other hand, is rich in  
350 these elements (77). Analysis of mantle xenoliths emplaced during and after eruption of the Siberian Traps demonstrates  
351 that the sub-continental lithospheric mantle stored abundant halogens, ~ 70% of which were scavenged by ascending  
352 melts (77). Therefore, destruction of the sub-continental lithospheric mantle and release of the volatiles it contains during  
353 LIP formation is a viable trigger for the P-T boundary extinction, and was probably enhanced by release of S and C  
354 from sediments as a result of magmatic heating (77–79). While it has been previously argued that destruction of the  
355 lithospheric mantle beneath the very largest LIPs contributes to the most significant mass extinction events, a temporal, if  
356 not mechanistic link has also been drawn between mass extinctions and smaller LIPs. For example, the Emeishan Traps,  
357 which are around  $\sim 3 \times 10^5 \text{ km}^3$  in volume (i.e. < 1/3 Siberian Traps), and erupted above the Yangtze Craton, have been  
358 linked to the end-Guadalupian mass extinction event (80, 81). Alteration and removal of the lithospheric mantle beneath  
359 even the smaller LIPs could therefore be a contributing factor to the environmental forcing that leads to mass extinction  
360 events.

## 361 Acknowledgements

362 SNS is supported by a research collaboration with Geoscience Australia. FDR is supported by an Imperial College  
363 Research Fellowship. The authors thank M. Hoggard, K. Czarnota, M. Klöcking, F. Mc Nab, C. O'Malley, K. Sigloch, D.  
364 Schutt, and N. White for their input and for many useful discussions.

## 365 Materials and Methods

### 366 Large Igneous Province Database

367 Coffin & Eldholm (38) and Coffin *et al.* (39) mapped the outlines of Phanerozoic large igneous provinces (LIPs) and  
 368 oceanic seamounts, and provided approximate eruption ages for each location. We have updated this database to include  
 369 LIPs up to 750 Ma. We further amended the ages and outlines of a number of polygons contained in the original database  
 370 to honor updated radiometric dates. A list of sources for the updated database can be found in the Supplementary Material.

### 371 Seismologic Estimates of Lithospheric Thickness

372 Throughout this study we exploit the lithospheric thickness model of Hoggard *et al.* (8). This model converts shear-wave  
 373 velocities,  $V_S$ , into temperature,  $T$  using the calibration method of Richards *et al.* (28) and the upper-mantle  $V_S$  tomographic  
 374 model of Schaeffer & Lebedev (82). This temperature conversion scheme relies on the experiment-based parameterisation  
 375 of Yamauchi & Takei (83), which accounts for the effects of anelasticity on  $V_S$  as the mantle melting temperature is  
 376 approached. The equations include seven material constants that are calibrated by exploiting the thermal structure beneath  
 377 mid-oceanic ridges in four different ways. First  $V_S$  profiles are extracted along oceanic plate flow lines and are averaged  
 378 to yield  $V_S$  as a function of plate age and depth. These stacked profiles are then compared to predicted values of  $V_S$  from  
 379 applying the  $V_S$ -to- $T$  conversion to a plate-cooling model (27). Misfit is calculated between observed and modeled  $V_S$   
 380 at depth slices of 87.5 and 112.5 km. Since oceanic plate thickness is generally  $\leq 125$  km, it is not possible to use this  
 381 approach at greater depths. Secondly,  $V_S$  profiles are averaged globally at depths beneath the thermal boundary layer (i.e.  
 382 between 225 and 400 km) and are compared to values of  $V_S$  predicted by applying the  $V_S$ -to- $T$  conversion to a mantle  
 383 isentrope with a potential temperature,  $T_p = 1333$  °C, which is assumed to represent ambient mantle. Thirdly, the globally  
 384 averaged shear wave attenuation as a function of depth beneath old ( $> 100$  Ma) oceanic lithosphere is calculated from  $V_S$   
 385 using the same conversion and compared to published estimates at depths  $> 150$  km. Finally, the misfit between published  
 386 and calculated depth-averaged mantle viscosity beneath the thermal boundary layer is evaluated.

387 These four misfit functions are combined, weighted and minimised to optimise the values of the seven unknown  
 388 material constants in the anelastic parameterisation. Finally, lithospheric thickness is calculated globally by extracting the  
 389 1175°C isotherm, which is assumed to be a proxy for the depth to the base of the mechanical boundary layer. For further  
 390 detail on the methodology, see Hoggard *et al.* (8) and Richards *et al.* (28).

### 391 Geochemical Estimates of Lithospheric Thickness

#### 392 Major Element Thermobarometry

393 Partitioning of major elements between melt and solid mantle is pressure and temperature dependent. The Plank &  
 394 Forsyth (29) thermobarometer exploits a comprehensive suite of melt-equilibration experiments to parameterise the  
 395 response of major-element composition to pressure and temperature changes. To estimate lithospheric thickness, we apply  
 396 this thermobarometer to a global database of Neogene–Quaternary mafic intraplate magmatic samples compiled by Ball  
 397 *et al.* (22). These calculations are carried out using meltPT – an open-source Python library designed for whole-rock  
 398 thermobarometric analysis [<https://github.com/fmcnab/meltPT>; (30, 84)].

399 Prior to estimating melt equilibration conditions, the effects of fractional crystallisation are mitigated by filtering  
 400 our magmatic database so that all samples have  $9 < \text{MgO} < 14.5$  wt%. Samples must also include a measurement of  
 401 Ce concentration so that  $\text{H}_2\text{O}$  can be estimated assuming that  $\text{H}_2\text{O}/\text{Ce} = 200$  (85, 86). We calculate the primary melt  
 402 compositions of each sample by adding olivine that is in equilibrium with the melt until olivine forsterite content is 0.9 (87).

403 Since only Fe<sup>2+</sup> is compatible within olivine, an estimate of Fe<sup>3+</sup>/ΣFe is required. We assume that Fe<sup>3+</sup>/ΣFe = 0.2, which  
404 is halfway between the average values for theolitic and alkali basalts (88).

405 These primary melt compositions are used to generate estimates of the pressure and temperature at which mantle  
406 melts equilibrated [i.e.  $P_{eq}$  and  $T_{eq}$ , respectively (29)]. Samples may have last equilibrated within the lithosphere or  
407 asthenosphere, and the boundary between these layers is defined throughout our study by the 1175 °C isotherm. In  
408 a given location, we assume that the maximum lithospheric thickness coincides with the equilibration pressure of the  
409 shallowest sample that has an equilibration temperature  $T_{eq} > 1175$  °C since temperatures cooler than this value are likely  
410 to indicate equilibration occurred within the lithosphere. To estimate lithospheric thickness globally, we subdivide our  
411 thermobarometric results into 1° × 1° geographic bins. We only estimate lithospheric thickness for bins with ≥ 10 samples  
412 since smaller sample sizes are less likely to capture the lithosphere–asthenosphere boundary.

#### 413 Rare Earth Element Inverse Modelling

414 We exploit the results of rare earth element (REE) inverse modeling presented by Ball *et al.* (22), who use an adapted  
415 form of the INVMEL-v12 forward model to simulate partitioning of trace elements between melt and residue within the  
416 mantle during melting (89). REE concentrations along adiabatic melt paths are calculated and misfit between observed  
417 and synthetic REE concentrations is minimised using a grid search procedure. Ball *et al.* (22) collect their data into  
418 1° × 1° geographic bins and calculate an optimum melt path for each bin. The upper limit of the melting region is assumed  
419 to represent the lithosphere–asthenosphere boundary (22). Note that this definition is slightly different to the isothermal  
420 definition used elsewhere in our study. The partitioning of each REE depends upon the bulk source composition, the  
421 aluminous phase present in the source, as well pressure and temperature. Ball *et al.* (22) filter their database for 8.5 <  
422 MgO < 14.5 wt% to mitigate fractionation effects, and they use  $\epsilon_{Nd}$  as a proxy for source composition. Finally, they place  
423 the garnet–spinel transition zone at 63–72 km (90).

## 424 Statistical Analyses

### 425 Weighted Median

426 In order to mitigate skewness and suppress outliers, we calculate the median when averaging data. For ease of analysis,  
427 we have divided Earth’s surface into 1° × 1° bins. To avoid oversampling higher latitudes and biasing median values, we  
428 weight each lithospheric thickness datapoint,  $z_i$ , by latitude,  $\phi_i$ . To achieve this weighting, we construct a data vector,  $\mathbf{z}$   
429 and a weights vector,  $\mathbf{w}$ , where each weight is given by  $\cos \phi_i$ . The weighted median is calculated by sorting  $\mathbf{z}$  and  $\mathbf{w}$   
430 in ascending order by the values of  $\mathbf{z}$ . The median value is given by  $z_j$ , where the index,  $j$ , of the sorted data vector is  
431 calculated by minimising

$$j = \min_k \left[ \sum_{i=1}^k w_i z_i > \frac{1}{2} \sum_{i=1}^n w_i z_i \right]. \quad (1)$$

432 For even-length data vectors, we use the upper-weighted median, so that  $z_j$  is given by  $(z_j + z_{j+1})/2$ . We calculate the  
433 weighted interquartile range of the distribution by changing the prefactor of  $\frac{1}{2}$  in Equation (1) to  $\frac{1}{4}$  and  $\frac{3}{4}$  for upper and  
434 lower quartiles, respectively.

### 435 Predicted Oceanic Lithospheric Thickness Distribution

436 Seamounts can only form on oceanic crust that is the same age, or older, than themselves. For example, a suite of seamounts  
437 erupting at the present day (i.e. 0 Ma) can cap oceanic crust that formed between the present day and Jurassic times. The  
438 median age of the sea floor beneath these seamounts will therefore lie somewhere between the two, and be skewed towards

439 younger ages since there is much more young oceanic crust than old on Earth (Figure 1a). Moreover, a seamount that is  
 440 200 Ma can only be located on crust  $\geq 200$  Ma, the majority of which has been subducted and lost from the surface record.  
 441 Consequently, since lithospheric plate thickness increases with age, we expect to observe a positive relationship between  
 442 seamount age and LAB depth.

443 Richards *et al.* (27, 28) constructed an oceanic plate-cooling model that simultaneously minimises the misfit between  
 444 global databases of heat flow and bathymetric observations that have been corrected for sediment and crustal loading.  
 445 Their approach includes both pressure- and temperature-dependent thermal properties. We assume that the LAB within  
 446 this plate-cooling model coincides with the 1175 °C isotherm [i.e. consistent with the LAB model of Hoggard *et al.* (8)].  
 447 We predict the unperturbed depth to the modern-day LAB,  $z_{LAB}^1$ , by extracting LAB depth as a function of age from  
 448 this plate model using the oceanic crustal age model of Muller *et al.* (31), which was updated to include additional data  
 449 by Richards *et al.* (27). The predicted value is compared to thickness implied by seismic tomography, which is in close  
 450 agreement [see Figure 1c; (8, 82)].

451 Oceanic crustal ages,  $t_{crust}$ , and LAB depths range from 0 Ma to  $t_{max}$  and from  $z_{LAB}(0)$  to  $z_{LAB}(t_{max})$ , respectively.  
 452 Seamounts cannot form on plates younger than their eruption age,  $t_e$ , and if  $t_e > t_{max}$ , then they would not be recorded  
 453 on Earth's surface today. Therefore, the thickness of lithosphere on which seamounts are located ranges from  $z_{LAB}(t_e)$   
 454 to  $z_{LAB}(t_{max})$ . For each eruption age, we record the lithospheric thickness distribution of oceanic crustal ages where  
 455  $t_e < t < t_{max}$ . The median and interquartile range of predicted lithospheric thickness as a function of  $t_e$  (i.e. the blue line  
 456 in 3d) is calculated using Equation (1).

## 457 Lithospheric Modelling

### 458 Parameterisation

459 To model lithospheric re-thickening following periods of active magmatism we solve the one-dimensional heat equation  
 460 expressed as

$$\rho(P, T, X)C_P(T, X)\frac{\partial T}{\partial t} = \frac{\partial}{\partial z}\left[k(P, T, X)\frac{\partial T}{\partial z}\right] + H^*(X), \quad (2)$$

461 where  $t$  is time,  $z$  is depth,  $T$  is temperature,  $P$  is pressure,  $X$  is composition,  $\rho$  is density,  $C_P$  is the isobaric specific heat  
 462 capacity,  $k$  is the thermal conductivity, and  $H^*$  is the internal radiogenic heat production.

463 Equation (2) is solved numerically with an unconditionally stable time- and space-centered Crank-Nicholson finite  
 464 difference scheme and a predictor-corrector step (91). Accordingly, Equation (2) is recast as

$$\begin{aligned} T_j^{n+1} + A &\left( -\frac{k_{j+\frac{1}{2}}^m}{\Delta z_j^m} T_{j+1}^{n+1} + \left( \frac{k_{j+\frac{1}{2}}^m}{\Delta z_j^m} + \frac{k_{j-\frac{1}{2}}^m}{\Delta z_{j-1}^m} \right) T_j^{n+1} - \frac{k_{j-\frac{1}{2}}^m}{\Delta z_{j-1}^m} T_{j-1}^{n+1} \right) \\ &= T_j^n + A \left( \frac{k_{j+\frac{1}{2}}^m}{\Delta z_j^m} T_{j+1}^n - \left( \frac{k_{j+\frac{1}{2}}^m}{\Delta z_j^m} + \frac{k_{j-\frac{1}{2}}^m}{\Delta z_{j-1}^m} \right) T_j^n + \frac{k_{j-\frac{1}{2}}^m}{\Delta z_{j-1}^m} T_{j-1}^n \right) + AH^* (\Delta z_j^m + \Delta z_{j-1}^m), \end{aligned} \quad (3)$$

465 where

$$A = \frac{\Delta t}{\left( \rho_j^m C_{Pj}^m (\Delta z_j^m + \Delta z_{j-1}^m) \right)}, \quad (4)$$

466 and  $\Delta t$  is the time step,  $\Delta z$  is the depth spacing between nodes, and  $n$  and  $j$  are the time and depth indices, respectively.  
 467 Equation (3) is solved by tridiagonal elimination (91). For the initial predictor phase of each time step,  $m = n$ , while in  
 468 the subsequent corrector phase,  $m = n + \frac{1}{2}$ . We use a Lagrangian reference frame, whereby  $\Delta z_j^m$  is initially set to 1 km  
 469 (i.e., when  $m = 0$ ) then scales with thermal contraction in subsequent timesteps. These timesteps are calculated using a

470 Courant-Friedrichs-Lowy condition calculated according to

$$\Delta t = \min_j \left[ \frac{\left( \Delta z_j^0 \right)^2 \rho_j^0 C_p^0}{2.2 k_j^0} \right] \sim 5 \text{ kyr.} \quad (5)$$

471  $T^{n+1}$  typically converges to within a tolerance of 0.001°C after the corrector phase.

## 472 Boundary Conditions

473 All models consist of crustal and mantle layers. Crustal thickness for oceanic and continental regions are set to  $z_{oc} = 20 \text{ km}$   
 474 and  $z_{cc} = 35 \text{ km}$ , respectively. In both cases the underlying mantle extends from the Moho to an assumed equilibrium plate  
 475 thickness,  $z_p$ . The initial depth to the LAB, after the cessation of magmatic activity and lithospheric thinning, is assumed  
 476 to be  $z_{LAB}^0 = 50 \text{ km}$ . To account for the possible presence of a mantle plume beneath the plate, initial asthenospheric  
 477 potential temperature,  $(T_p)_0$ , can vary between 1333°C, which is assumed to be the temperature of ambient mantle, and  
 478 1633°C (i.e. an excess temperature of 300 °C).

479 Separate parameterisations are used to define the thermophysical properties of the crust and mantle ( $k$ ,  $C_p$ ,  $\rho$ , and  
 480  $H^*$ ). Crustal radiative thermal conductivity and  $\rho$  are determined using the Richards *et al.* (46) parameterisation, but the  
 481 reference density,  $\rho_0$ , is dependent on whether oceanic or continental lithosphere is to be modelled (2950 kg m<sup>-3</sup> and  
 482 2700 kg m<sup>-3</sup>, respectively). In the continental crust,  $C_p$  and lattice thermal diffusivity,  $\kappa_{lat}$ , are calculated using the  
 483 parameterisation of Whittington *et al.* (48), and  $H^*$  is assumed to be 0.7 μW m<sup>-3</sup> (8). In oceanic crust, we use the Richards  
 484 *et al.* (46) parameterisation for  $C_p$  and  $\kappa_{lat}$ , and assume  $H^* = 0 \text{ mW m}^{-3}$ . In both the continental and oceanic mantle,  
 485 the temperature- and pressure-dependent formulations specified in Richards *et al.* (46) are adopted, with radiogenic heat  
 486 production assumed to be negligible ( $H^* = 0 \mu\text{W m}^{-3}$ ).

487 Initial temperature profiles are obtained by combining the parameters outlined above with the equations of M<sup>c</sup>Kenzie  
 488 *et al.* (92). In all cases kinematic viscosity,  $\nu$ , is assumed to be  $9 \times 10^{19} \text{ m}^2 \text{ s}^{-1}$ . For each combination of  $z_{oc}$  or  $z_{cc}$ , and  
 489  $(T_p)_0$ , we find the steady-state geotherm consistent with  $z_{LAB}^0$  by iterating through a range of mechanical boundary layer  
 490 thicknesses (2–60 km). We select the temperature profile with depth to the 1175°C isotherm equal to  $z_{LAB}^0$ .

491 To simulate the waning of a plume-derived heat source through time, we impose an evolving basal boundary condition.  
 492 At  $t = 0$ ,  $T(z)$  is given by the initial isentrope defined by  $(T_p)_0$  below the base of the thermal boundary layer (i.e., the  
 493 shallowest depth at which the geothermal gradient,  $\frac{\partial T}{\partial z}$ , drops below 0.5°C km<sup>-1</sup>). In later timesteps, the depth at which  
 494 this boundary condition is imposed,  $z_b$ , increases according to a prescribed plume sinking rate,  $v_{plume} = 10 \text{ mm yr}^{-1}$ , until  
 495 the deepest model node (i.e.  $z_b = z_p$ ) is reached, whereupon the basal boundary depth remains fixed. Simultaneously,  
 496 from  $t = 0$ –30 Myr, the temperature applied at the basal boundary decays linearly to that of the ambient mantle isentrope  
 497 (i.e.  $T_p = 1333 \text{ }^\circ\text{C}$ ) at the relevant depth. Beyond  $t = 30 \text{ Myr}$ , the basal temperature is assumed to remain equal to that of  
 498 the ambient mantle isentrope at the appropriate depth.

## 499 Optimisation Strategy

500 We carry out a two-parameter sweep to find the combination of plate thickness,  $z_p$ , and initial potential temperature,  $(T_p)_0$ ,  
 501 that best explains our constraints on  $z_{LAB}(t)$ . For each  $(z_p, (T_p)_0)$  pair we find the initial steady-state thermal structure  
 502 that yields  $z_{LAB}^0 = 50 \text{ km}$ . Note that, if the lithospheric mantle is instantaneously thinned, it is likely that the remaining  
 503 mantle will not be thermally equilibrated. Nonetheless, since the conductive layer is thin, it will rapidly reach steady state  
 504 and so the effect of thermal disequilibrium is likely to be minor. We then calculate  $z_{LAB}(t)$ , for  $0 < t < t_{max}$  Ma, where  
 505  $t_{max} = 750 \text{ Ma}$ , using Equation (3). To minimise the misfit between tomographically determined LAB depth and predicted  
 506 LAB depth as a function of age beneath LIPs, we use the trial function

$$\chi = \sqrt{\frac{1}{M} \sum_{i=1}^M \left( \frac{z_i^o - z_i^c}{\sigma_i} \right)^2}, \quad (6)$$

507 where  $z_i^o$  and  $z_i^c$  are observed and calculated LAB depth,  $\sigma_i$  is the standard deviation of the  $i^{\text{th}}$  measurement, and  $M$  is the  
 508 number of estimates. We used weighted binned median lithospheric thickness estimates, where

$$\sigma_i = \frac{\sqrt{(\text{IQR}_1^i)^2 + (\text{IQR}_2)^2}}{1.349}, \quad (7)$$

509 and  $\text{IQR}_1^i$  is the interquartile range of the  $i^{\text{th}}$  measurement and  $\text{IQR}_2 = 25$  km is the approximate vertical uncertainty of  
 510 the lithospheric thickness grid. Note that this relationship assumes that errors are normally distributed.

## 511 Subsidence

512 Air-loaded subsidence of the surface for our pressure- and temperature-dependant plate model is given by

$$S(t) = \int_0^{z_p} \left[ 1 - \frac{\rho(0, z')}{\rho(t, z')} \right] dz', \quad (8)$$

513 where  $z'$  is the Lagrangian depth coordinate that deepens as the column is compressed. The effect of lithospheric depletion  
 514 is explored by adding  $\Delta\rho$  (i.e.  $\Delta\rho$  is negative for more depleted lithosphere) to all values of  $\rho(t, z')$  that are located at  
 515 depths,  $z$ , within the lithospheric mantle (i.e.  $z_{cc} < z < z_{LAB}$ ). Since many ancient LIPs are located above continental  
 516 shields, we assume that the pre-LIP lithospheric mantle was in thermal equilibrium, initially cratonic, and depleted by  
 517  $\Delta\rho = 50 \text{ Mg m}^{-3}$  (Figure 4a). We explore initial geotherms that are out of equilibrium in the Supplementary Material.  
 518 For simplicity, we assume that the steady-state thermal structure of the lithospheric column before thinning and after  
 519 re-thickening are identical and given by the results of our thermal evolution modelling (i.e.  $z_{LAB}^\infty$ ; Figure 3d). Initial  
 520 uplift,  $U_o = S(0)$ , after thinning is calculated using Equation(8), thence  $S(t)$  is calculated using a range of values of  $\Delta\rho$   
 521 to explore the effect of lithospheric melt depletion upon subsidence of the Earth's surface (Figure 4).

---

522

## 523 References

- 524 1. D. M<sup>c</sup>Kenzie, M. J. Bickle, *Journal of Petrology* **29**, 625 (1988).
- 525 2. S. D. King, D. L. Anderson, *Earth and Planetary Science Letters* **160**, 289 (1998).
- 526 3. A. B. Watts, *Isostasy and flexure of the lithosphere* (Cambridge University Press, Cambridge, 2001).
- 527 4. N. H. Sleep, *Journal of Geophysical Research: Solid Earth* **108** (2003).
- 528 5. A. Lenardic, L.-N. Moresi, A. Jellinek, M. Manga, *Earth and Planetary Science Letters* **234**, 317 (2005).
- 529 6. P. Molnar, P. England, *nature* **346**, 29 (1990).
- 530 7. P. B. Wignall, *Earth-science reviews* **53**, 1 (2001).
- 531 8. M. J. Hoggard, *et al.*, *Nature Geoscience* **13**, 504 (2020).
- 532 9. M. J. Hoggard, J. Austermann, C. Randel, S. N. Stephenson, *Mantle convection and surface expressions* pp. 371–411 (2021).
- 533 10. B. Parsons, J. G. Sclater, *Journal of geophysical research* **82**, 803 (1977).
- 534 11. J. Jackson, D. M<sup>c</sup>Kenzie, K. Priestley, B. Emmerson, *Journal of the Geological Society* **165**, 453 (2008).
- 535 12. W. Griffin, S. Y. O’reilly, J. C. Afonso, G. Begg, *Journal of Petrology* **50**, 1185 (2009).
- 536 13. M. E. Pasyanos, T. G. Masters, G. Laske, Z. Ma, *Journal of Geophysical Research: Solid Earth* **119**, 2153 (2014).
- 537 14. J. C. Afonso, *et al.*, *Journal of Geophysical Research: Solid Earth* **121**, 7337 (2016).
- 538 15. M. Klöcking, *et al.*, *Earth and Planetary Science Letters* **547**, 116464 (2020).
- 539 16. D. G. Pearson, *et al.*, *Nature* **596**, 199 (2021).
- 540 17. T. H. Jordan, *Nature* **274**, 544 (1978).
- 541 18. P. F. Hoffman, *Annual Review of Earth and Planetary Sciences* **16**, 543 (1988).
- 542 19. C. O’Neill, A. Lenardic, W. L. Griffin, S. Y. O'Reilly, *Lithos* **102**, 12 (2008).
- 543 20. R. E. Ernst, *et al.*, *Large igneous provinces: A driver of global environmental and biotic changes* pp. 1–26 (2021).
- 544 21. N. L. Celli, S. Lebedev, A. J. Schaeffer, M. Ravenna, C. Gaina, *Geophysical Journal International* **221**, 178 (2020).
- 545 22. P. W. Ball, N. J. White, J. Maclennan, S. N. Stephenson, *Nature Communications* **12**, 1 (2021).
- 546 23. Y. Niu, *Earth-Science Reviews* **217**, 103614 (2021).
- 547 24. J. Liu, *et al.*, *Nature* **592**, 732 (2021).
- 548 25. M. Stein, A. W. Hofmann, *Earth and Planetary Science Letters* **114**, 193 (1992).
- 549 26. J. Afonso, G. Ranalli, M. Fernandez, *Geophysical Research Letters* **34** (2007).
- 550 27. F. D. Richards, M. J. Hoggard, L. Cowton, N. J. White, *Journal of Geophysical Research: Solid Earth* **123**, 9136 (2018).
- 551 28. F. D. Richards, M. J. Hoggard, N. J. White, S. Ghelichkhane, *Journal of Geophysical Research: Solid Earth* p. e2019JB019062 (2020).
- 553 29. T. Plank, D. Forsyth, *Geochemistry, Geophysics, Geosystems* **17**, 1312 (2016).
- 554 30. F. M<sup>c</sup>Nab, P. W. Ball, *Volcanica* (in press).
- 555 31. R. D. Müller, N. Flament, K. J. Matthews, S. E. Williams, M. Gurnis, *Earth and Planetary Science Letters* **441**, 60 (2016).
- 556 32. F. A. Darbyshire, I. T. Bjarnason, R. S. White, Ó. G. Flóvenz, *Geophysical Journal International* **135**, 1131 (1998).
- 557 33. J. Jenkins, *et al.*, *Journal of Geophysical Research: Solid Earth* **123**, 5190 (2018).
- 558 34. B. M. Le, T. Yang, J. P. Morgan, *Journal of Geophysical Research: Solid Earth* p. e2021JB023822 (accepted).
- 559 35. N. Schmerr, *Science* **335**, 1480 (2012).
- 560 36. I. Guest, G. Ito, M. O. Garcia, E. Hellebrand, *Geochemistry, Geophysics, Geosystems* **21**, e2020GC009359 (2020).
- 561 37. A. Pleus, G. Ito, P. Wessel, L. N. Frazer, *Geophysical Journal International* **222**, 207 (2020).
- 562 38. M. F. Coffin, O. Eldholm, *Reviews of Geophysics* **32**, 1 (1994).
- 563 39. M. F. Coffin, *et al.*, *Oceanography* **19**, 150 (2006).
- 564 40. C. A. Stein, S. Stein, *Journal of Geophysical Research: Solid Earth* **99**, 3081 (1994).
- 565 41. C. J. Grose, J. C. Afonso, *Geochemistry, Geophysics, Geosystems* **14**, 3751 (2013).
- 566 42. R. S. Detrick, S. T. Crough, *Journal of Geophysical Research: Solid Earth* **83**, 1236 (1978).
- 567 43. R. White, D. McKenzie, *Journal of Geophysical Research: Solid Earth* **100**, 17543 (1995).

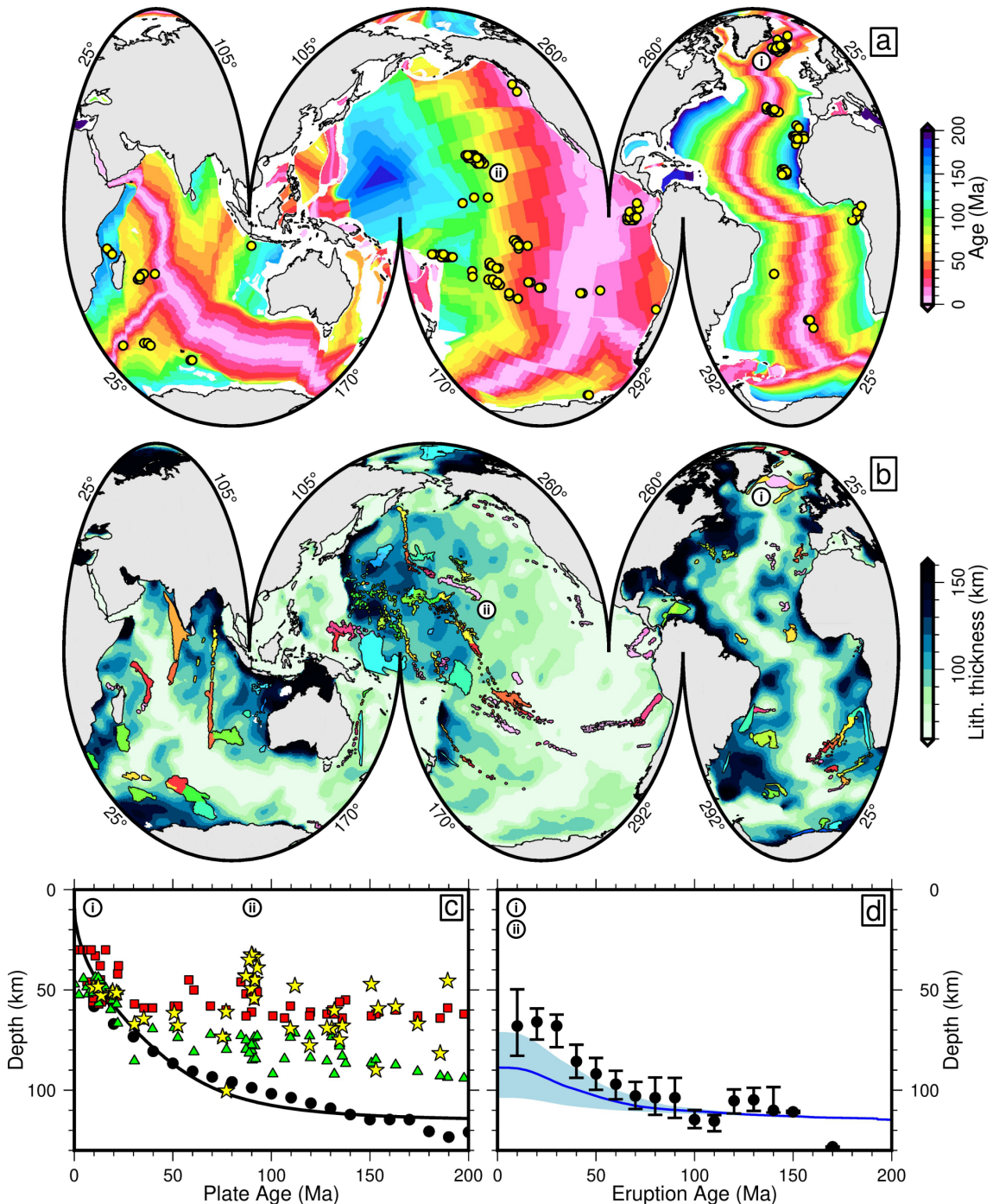


**Figure 1: Distribution of oceanic magmatic provinces.** (a) Oceanic plate age (31, 93). Yellow circles = locations of intraplate magmatic provinces (22); (i) & (ii) = locations of Icelandic and Hawaiian hotspots. (b) Oceanic LAB depth (8). Coloured polygons = locations of oceanic magmatic provinces (i.e. ocean islands, seamounts and plateaux) coloured by age. (c) Constraints on modern-day LAB depth beneath intraplate magmatic provinces as a function of underlying oceanic crustal age. Red squares = LAB depth determined by inverse modelling of rare earth element compositions of mafic rocks (22); green triangles = thickness determined by tomographic-derived LAB depth model shown in panel (b) (8, 82); yellow stars = LAB depth estimated by finding magmatic equilibration pressure and temperature that corresponds to base of lithosphere (this study, see main text & Methods); (i) & (ii) = age of plate underlying Icelandic and Hawaiian hotspots. (d) Black circles with error bars = modern LAB depth beneath magmatic provinces as a function of province age; moving median at 10 Ma intervals with a  $\pm 20$  Myr window; error bars = interquartile range; blue line = median expected distribution of LAB depth beneath LIPs if they were distributed randomly in time and space across oceanic lithosphere assuming plate model of Richards *et al.* (28) and plate age model of Muller *et al.* (31); blue envelope = interquartile range; (i) & (ii) = age of Icelandic and Hawaiian hotspots.

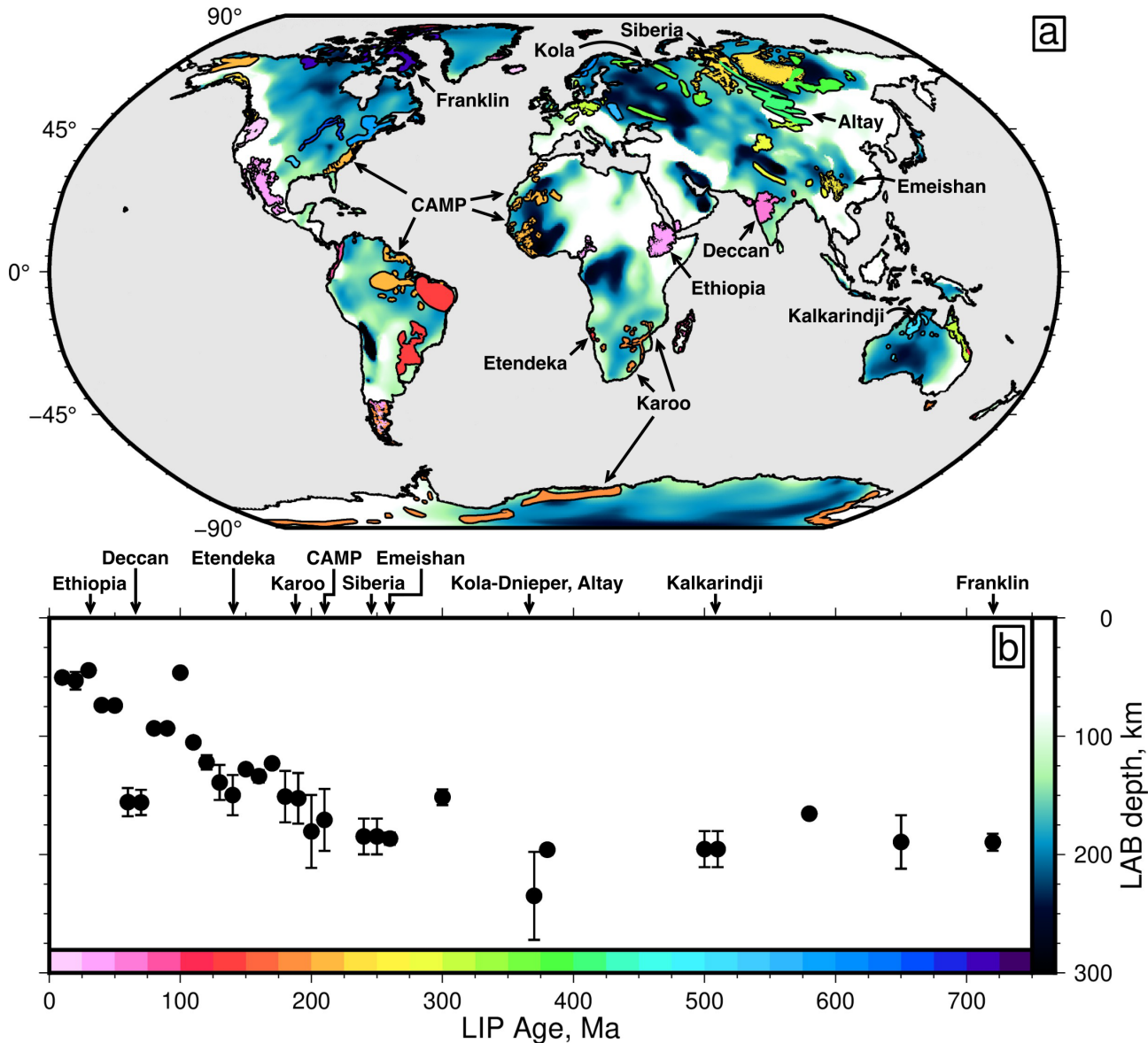
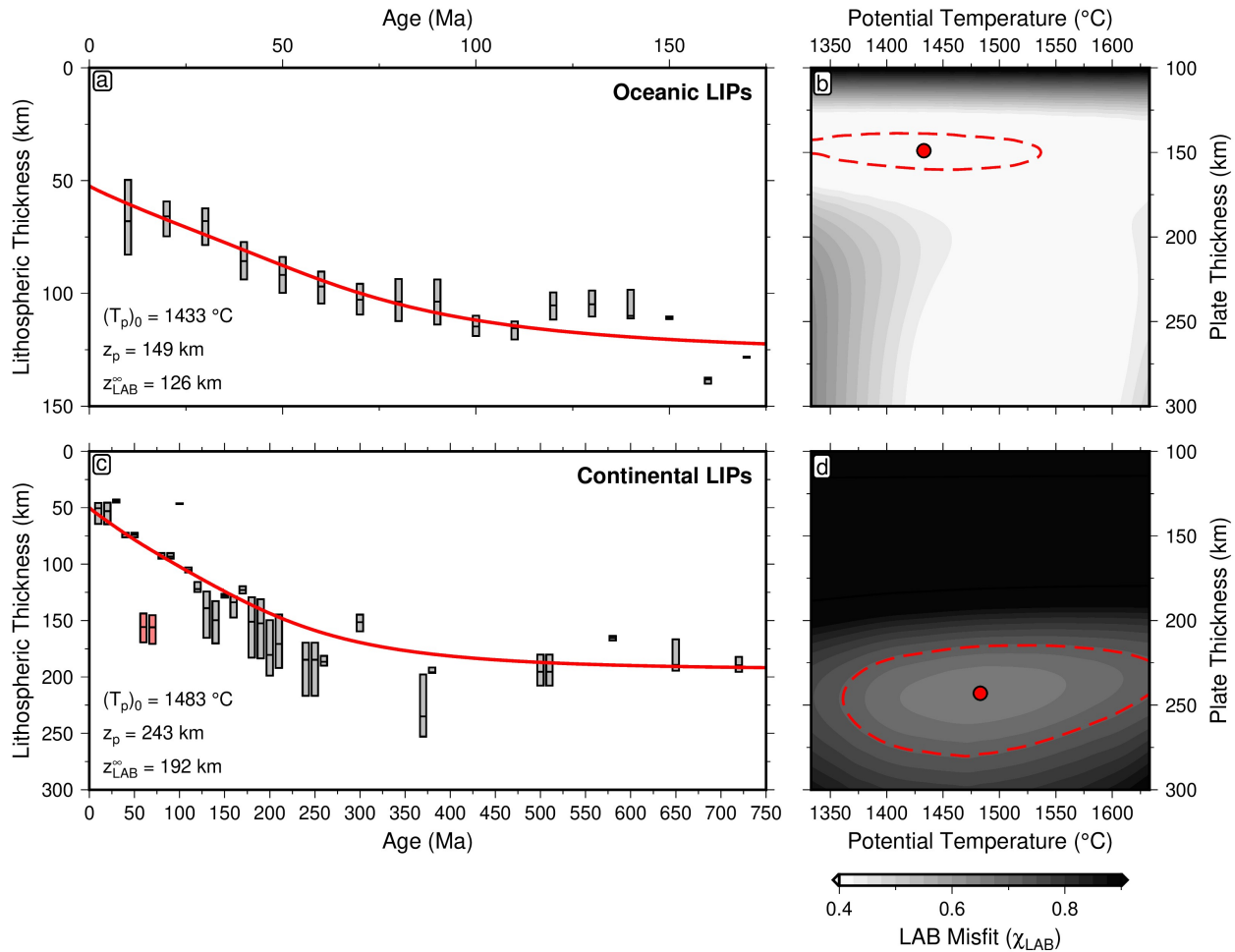
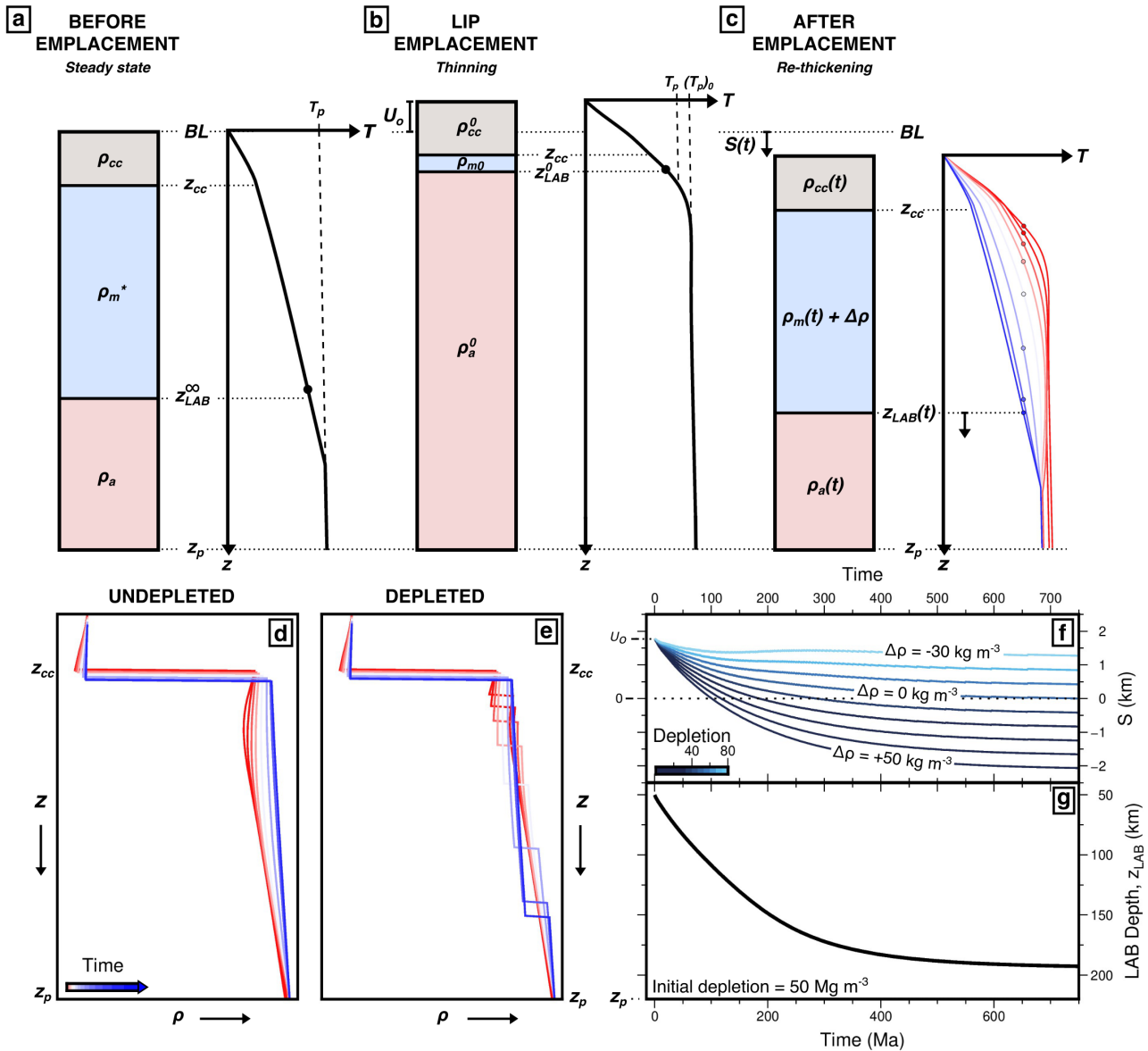


Figure 2: **Global distribution of continental large igneous provinces.** (a) Distribution of continental large igneous provinces in space and time overlain on map of continental LAB depth (8). Scale bars located on axes of panel (b); labels indicate names of LIPs mentioned in the main text. (b) Modern-day LAB depth beneath large igneous provinces as a function of LIP age (8). Labels indicate age of LIPs mentioned in main text.



**Figure 3: Lithospheric thermal modelling.** (a) Observed and modelled LAB depth beneath oceanic intraplate magmatic provinces as function of eruptive age. Grey bar = interquartile range of LAB depth distribution; red line = best-fitting modelled LAB depth.  $(T_p)_0$  = initial potential temperature;  $z_p$  = plate thickness;  $z_{\text{LAB}}^{\infty}$  = asymptotic depth to the LAB as  $t \rightarrow \infty$ . (b) Misfit between observed and calculated LAB depth as function of plate thickness,  $z_p$ , and initial potential temperature,  $(T_p)_0$ , for oceanic intraplate magmatism (see methods for details). Red circle = misfit minimum; red dashed line = contour marking 1.5 $\times$  value at misfit minimum. Optimum values given in lower left-hand corner of panel (a). (c) Observed and modelled LAB depth beneath continental LIPs as function eruptive age. Red bars = Deccan Traps, excluded from the analysis. (d) As panel (b) but for continental LIPs. Optimum values given in lower left-hand corner of panel (c).



**Figure 4: Thermal, depletion and subsidence modeling.** (a) Pair of cartoons showing continental column and temperature profile of precursory lithosphere before LIP emplacement. Lithosphere initially in thermal steady-state.  $z_{LAB}^\infty$  = steady-state lithosphere-asthenosphere boundary (LAB) depth, defined by 1175°C isotherm;  $z_{cc}$  = crustal thickness;  $z_p$  = plate thickness;  $\rho_{cc}$  = steady-state crustal density;  $\rho_m^*$  = steady-state initial lithospheric mantle density;  $\rho_a$  = steady-state asthenospheric density;  $T_p$  = ambient mantle potential temperature;  $BL$  = base level (i.e. initial elevation of top of lithospheric column). (b) Perturbed (i.e. thinned) lithospheric column during LIP emplacement at  $t = 0$ , where LAB depth,  $z_{LAB}^0 = 50$  km;  $U_o$  = initial uplift driven by thinning of the plate and sub-plate thermal anomaly;  $\rho_m^0$  = initial lithospheric mantle density;  $\rho_a^0$  = initial asthenospheric mantle density;  $(T_p)_0$  = initial (i.e. elevated) mantle potential temperature. (c) Subsidence as LAB depth,  $z_{LAB}(t)$ , deepens from  $z_{LAB}^0$  back to  $z_{LAB}^\infty$ .  $\rho_{cc}(t)$  = crustal density as function of time;  $\rho_m(t)$  = lithospheric mantle density as function of time;  $\rho_a(t)$  = asthenospheric mantle density as function of time;  $\Delta\rho$  = difference as result of depletion between precursor,  $\rho_m^*$ , and final lithospheric mantle density,  $\rho_m^\infty$ ;  $S(t)$  = time-dependent net subsidence (i.e. above or below base level,  $BL$ ), where  $S(\infty) = 0$  km if  $\Delta\rho = 0 \text{ Mg m}^{-3}$ . (d) Density as function of depth for thickening of undepleted lithospheric mantle coloured by time (i.e. blue to red through time). (e) As for (d) but with depleted lithospheric mantle (i.e. density reduction relative to ambient mantle,  $\Delta\rho = -50 \text{ kg m}^{-3}$ ). (f) Air-loaded subsidence as function of time,  $S(t)$ , for various values of  $\Delta\rho$  after thinning precursory lithosphere from  $z_{LAB}^\infty = 200$  km to  $z_{LAB}^0 = 50$  km with initial depletion of  $-50 \text{ kg m}^{-3}$ .  $U_o = 1.76$  km is transient initial uplift generated by combined effect of thinning depleted precursory lithosphere and sub-plate thermal anomaly. Note that if re-thickening lithosphere is more depleted than original lithosphere then uplift is generated after steady-state is re-achieved. Dotted line = no net uplift or subsidence. Labelled lines indicate values of  $\Delta\rho$  where negative values are density reductions due to increased depletion. (g) Depth to LAB as a function of time,  $z_{LAB}(t)$ .

- 568 44. S. Fishwick, *Lithos* **120**, 63 (2010).
- 569 45. A. Davaille, C. Jaupart, *Journal of Geophysical Research: Solid Earth* **99**, 19853 (1994).
- 570 46. F. Richards, M. Hoggard, A. Crosby, S. Ghelichkhan, N. J. White, *Physics of the Earth and Planetary Interiors* **309**, 106559 (2020).
- 571 47. K. L. Huppert, J. T. Perron, L. H. Royden, *Science advances* **6**, eaaw6906 (2020).
- 572 48. A. G. Whittington, A. M. Hofmeister, P. I. Nabelek, *Nature* **458**, 319 (2009).
- 573 49. A. D. Saunders, R. W. England, M. K. Reichow, R. V. White, *Lithos* **79**, 407 (2005).
- 574 50. A. Saunders, *et al.*, *Chemical Geology* **241**, 282 (2007).
- 575 51. R. Newman, N. J. White, *Philosophical Transactions of the Royal Society of London. Series A: Mathematical, Physical and Engineering Sciences* **357**, 805 (1999).
- 577 52. J. J. Armitage, P. A. Allen, *Journal of the Geological Society* **167**, 61 (2010).
- 578 53. C.-T. A. Lee, P. Luffi, E. J. Chin, *et al.*, *Annual Review of Earth and Planetary Sciences* **39**, 59 (2011).
- 579 54. P. Bird, *Journal of Geophysical Research: Solid Earth* **84**, 7561 (1979).
- 580 55. D. M<sup>c</sup>Kenzie, *Earth and Planetary science letters* **40**, 25 (1978).
- 581 56. B. He, Y.-G. Xu, S.-L. Chung, L. Xiao, Y. Wang, *Earth and Planetary Science Letters* **213**, 391 (2003).
- 582 57. I. H. Campbell, *Elements* **1**, 265 (2005).
- 583 58. X. Wang, *et al.*, *Earth-science reviews* **207**, 103224 (2020).
- 584 59. S. N. Stephenson, *et al.*, *Geochemistry, Geophysics, Geosystems* **22**, e2020GC009624 (2021).
- 585 60. A. Sembroni, C. Faccenna, T. W. Becker, P. Molin, B. Abebe, *Tectonics* **35**, 469 (2016).
- 586 61. K. Luszczak, C. Persano, F. Stuart, *Tectonics* **37**, 914 (2018).
- 587 62. K. L. Buchan, *et al.*, *Dyke swarms: time markers of crustal evolution* pp. 27–48 (2006).
- 588 63. K. L. Buchan, R. E. Ernst, *Gondwana Research* **58**, 39 (2018).
- 589 64. J. Brodie, N. J. White, *Geology* **22**, 147 (1994).
- 590 65. D. M<sup>c</sup>Kenzie, F. M. Richter, *Journal of Geophysical Research: Solid Earth* **86**, 11667 (1981).
- 591 66. G. Hirth, D. L. Kohlstedt, *Earth and Planetary Science Letters* **144**, 93 (1996).
- 592 67. G. Hirth, D. L. Kohlstedt, *Geophysical monograph-american geophysical union* **138**, 83 (2003).
- 593 68. T. Stachel, R. Luth, *Lithos* **220**, 200 (2015).
- 594 69. J. Sun, *et al.*, *Earth and Planetary Science Letters* **404**, 283 (2014).
- 595 70. K. Smit, T. Stachel, R. Stern, *Contributions to Mineralogy and Petrology* **167**, 1 (2014).
- 596 71. H. Helmstaedt, J. Gurney, *Journal of Geochemical Exploration* **53**, 125 (1995).
- 597 72. R. E. Ernst, D. R. Davies, S. M. Jowitt, I. Campbell, *Earth and Planetary Science Letters* **502**, 244 (2018).
- 598 73. H. Sigurdsson, *Global and Planetary Change* **3**, 277 (1990).
- 599 74. B. A. Black, L. T. Elkins-Tanton, M. C. Rowe, I. U. Peate, *Earth and Planetary Science Letters* **317**, 363 (2012).
- 600 75. S. Callegaro, *et al.*, *Geology* **42**, 895 (2014).
- 601 76. S. M. Stanley, *Proceedings of the National Academy of Sciences* **113**, E6325 (2016).
- 602 77. M. W. Broadley, P. H. Barry, C. J. Ballentine, L. A. Taylor, R. Burgess, *Nature Geoscience* **11**, 682 (2018).
- 603 78. C. Ganino, N. T. Arndt, *Geology* **37**, 323 (2009).
- 604 79. J. Guex, *et al.*, *Scientific reports* **6**, 1 (2016).
- 605 80. M.-F. Zhou, *et al.*, *Earth and Planetary Science Letters* **196**, 113 (2002).
- 606 81. J. G. Shellnutt, *Geoscience Frontiers* **5**, 369 (2014).
- 607 82. A. J. Schaeffer, S. Lebedev, *Geophysical Journal International* **194**, 417 (2013).
- 608 83. H. Yamauchi, Y. Takei, *Journal of Geophysical Research: Solid Earth* **121**, 7790 (2016).
- 609 84. F. M<sup>c</sup>Nab, P. W. Ball, meltPT: Preliminary release (v0.0.2-alpha), Zenodo <https://doi.org/10.5281/zenodo.6948031> (2022).
- 610 85. J. E. Dixon, L. Leist, C. Langmuir, J.-G. Schilling, *Nature* **420**, 385 (2002).
- 611 86. F. M<sup>c</sup>Nab, P. W. Ball, M. J. Hoggard, N. J. White, *Geochemistry, Geophysics, Geosystems* **19**, 175 (2018).
- 612 87. C. T. A. Lee, P. Luffi, T. Plank, H. Dalton, W. P. Leeman, *Earth and Planetary Science Letters* **279**, 20 (2009).

- 613 88. D. Canil, R. D. Hyndman, D. Fode, *Geophysical Research Letters* **48**, e2020GL091957 (2021).
- 614 89. D. M<sup>c</sup>Kenzie, R. K. O'Nions, *Journal of Petrology* **32**, 1021 (1991).
- 615 90. E. S. Jennings, T. J. B. Holland, *Journal of Petrology* **56**, 869 (2015).
- 616 91. W. H. Press, S. A. Teukolsky, W. T. Vetterling, B. P. Flannery, *Numerical recipes 3rd edition: The art of scientific computing* (Cambridge university press, 2007).
- 617
- 618 92. D. M<sup>c</sup>Kenzie, J. Jackson, K. Priestley, *Earth and Planetary Science Letters* **233**, 337 (2005).
- 619 93. M. J. Hoggard, J. Winterbourne, K. Czarnota, N. J. White, *Journal of Geophysical Research: Solid Earth* **122**, 2328 (2017).